Bulk flow model for multislice magnetic resonance imaging sequences with phantom validation

Charles R. Meyer and David M. Williams
Department of Radiology, University of Michigan Hospitals, Ann Arbor, Michigan 48109

(Received 10 March 1987; accepted for publication 30 September 1987)

A simple conceptual model for describing the effects of one-dimensional bulk flow on image intensities is presented and validated using a multislice imaging sequence specific to one vendor. The model allows quantitative estimates of echo amplitudes versus velocity by using the equation of motion to follow the pulse history of fluid volumes influenced by the readout pulse for any slice of interest. Each affected volume is divided into equal elemental components and the state of each component is computed at discrete times in a pulse position-timing diagram until readout occurs. The final amplitude for the composite volume is determined by the signed summation of each of the elemental components. Validation of the quantitative model was performed by imaging a rotating bulk flow phantom centered at each of the slices of a multislice, partial saturation, spin-echo sequence. Effects due to rf field inhomogeneities were normalized by dividing the results of the dynamic scans by the corresponding static one. The results presented here are relatively insensitive to odd-echo dephasing (even echo rephasing).

I. INTRODUCTION

Most clinicians are using standard, vendor supplied multislice acquisition sequences for routine, diagnostic magnetic resonance imaging. While the literature adequately describes flow effects seen in single slice techniques,[1,2] as well as new acquisition sequences which selectively enhance and/or quantitate flow,[3–8] little has been published regarding multislice flow effects in vendor supplied sequences.[9] Understanding of the wide range of such effects can improve the clinician's diagnostic accuracy in flow related questions such as differentiating thrombus versus patency.[10] Since flow in major vessels is often parallel to the long axis of the patient, referred to hereafter as the z axis, and is typically viewed in transaxial cross section, we will concentrate on z-axis, nonpulsatile flow as seen in transaxial slices for the remainder of this paper. Although the general modeling concept we develop here is validated by applying it to the case of a partial saturation, spin-echo sequence of a specific vendor, application of the technique to other pulse sequences should be obvious. Other simplifying assumptions include considering selective rf pulse profiles to be entirely uniform with respect to flip angle over the full spatial extent of the selected region, and zero outside. Such approximations are more easily justified for selective 90° pulses than 180° pulses,[11] but even so, the model performs surprisingly well. Since rf pulse durations are typically very short with respect to echo evolution times, we assume pulse durations to be infinitesimally small.

II. MODEL

Modeling of bulk flow effects for many commercially available imaging sequences can be achieved by the use of a generalized pulse position-timing diagram similar to Fig. 1 in combination with the equation of motion for the material. The ordinate describes z-axis position and the abscissa represents time. The specific diagram presented here and used throughout the remainder of this paper was drawn using the imaging parameters for a Diasonics 0.35 T system using a five slice partial saturation, spin-echo (two echo) sequence, but could be easily redrawn to reflect imaging sequences used by other vendors. Figure 1 shows the correct placement with respect to location and time of both 90° and 180° pulses for two repetitions of a five slice partial saturation, spin-echo (two echo) sequence, where the $T_r = 0.5$ s and $T_e = 28$ and 56 ms. For this diagram the 180° refocusing pulses occur and are plotted at 14 and 42 ms after the 90° pulse. Center-to-center slice separations are 1 cm, and the slice width is 0.6 cm for the 90° pulse, and 1.0 cm for the 180° pulse. For those readers familiar with the usual sequence timing diagram presented in most papers, it should be clear that the only information missing in Fig. 1 is the time of occurrence of the y-axis (phase warping) and x-axis (readout) gradients. In fact, Fig. 1 presents more information than the usual one cycle sequence which shows only time of occurrence of gradients and rf pulses. In Fig. 1 both complete timing and resulting spatial relationships for the interaction of the z-axis gradients and rf induced flip angles are shown. Note that by tracing the rf pulse sequence for any slice in Fig. 1, the usual

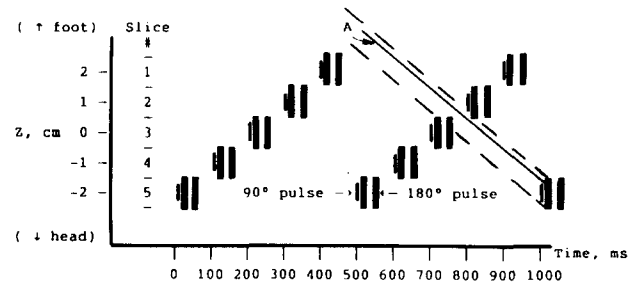

FIG. 1. Pulse position-timing diagram showing the placement with respect to location and time of both 90° and 180° pulses for two repetitions of a five slice partial saturation, spin-echo sequence for a Diasonics 0.35 T imager, where the $T_r = 0.5$ s and $T_e = 28$ and 56 ms. For this diagram the 180° refocusing pulses occur at 14 and 42 ms after the 90° pulse. Center-to-center slice separations are 1 cm, and the slice width is 0.6 cm for the 90° pulse, and 1.0 cm for the 180° pulse. Line A demonstrates an elemental volume traveling at − 10 cm/s that passes through the first refocusing pulse of slice 5.

 0094-2405/88/010001-06$01.20

partial saturation, two echo spin-echo sequence, i.e., —90°-T_e/2-180°-T_e/2-readout-T_e/2-180°-T_e/2- readout—(T_r-2T_e)], is obtained.

Since the diagram is a plot of z-axis position versus time, an elemental volume flowing with constant velocity describes a straight line on the diagram where the slope of the line is equal to its z-axis velocity. For static material the slope is zero, i.e., a horizontal line. The solid straight line labeled A in Fig. 1 depicts an elemental volume traveling with constant velocity of − 10 cm/s that is influenced by the first of two 180° refocusing pulses of slice 5. Note that the elemental volume has not been influenced by any other pulses prior to experiencing the 180° pulse, and thus will not contribute any signal during first echo readout since none of that volume's spins are in the transverse plane at readout. However to estimate the amplitude of any echo for material traveling at constant velocity, we must estimate the signed (phase) contribution of all elemental volumes influenced by that echo's 180° refocusing pulse. The loci of such elemental volumes for the first echo of slice 5 are depicted in Fig. 1 within the dashed lines. Note that some of the volumes are affected by the 180° pulses of slice 3 in the previous repetition period while a smaller fraction are affected by the 90° pulse of slice 5. The resulting echo amplitude is the summed effect of all of the elemental volumes. By further observation of Fig. 1 the reader can easily envision other possible ranges of material velocities where the resulting echo for slice 5 is likely to be larger than that for similar stationary material because the vertical spins reaching the readout sequence have recovered more than if they were stationary. Others have used a similar diagram without the 180° refocusing pulses for similar descriptive purposes without further pursuit of quantitative echo amplitudes.[9]

Quantitative estimation of echo amplitudes for bulk material moving at constant velocity can be achieved by a number of methods suggested by the pulse position-timing diagram. We chose to use a finite element computer model which divided the spatial extent of the desired 180° refocusing pulse for any slice of interest into 50 elemental volumes, and followed the state of each elemental volume through five previous pulse repetition periods before computing the resulting echo amplitude. A two-dimensional array was used to compute the state of the vertical and transverse spins with respect to time for each elemental volume, where one dimension corresponded to elemental volume location and the other corresponded to time. We found that 50 elemental volumes were necessary to reduce quantization error in the resulting plots of echo amplitude versus velocity, and that five repetition periods were sufficient to approximate steady-state conditions for stationary material. For a given echo and slice of interest an outer program loop incremented velocity in finite increments from $-V_{max}$ to $+V_{max}$. For each velocity the two-dimensional array was populated with 0's, 1's, and 2's corresponding to the absence of any rf pulse, the presence of a 90° pulse, or the presence of a 180° pulse, respectively, in each elemental volume based on the time of pulse occurrence and the material's equation of motion, i.e., velocity and final position of the elemental volume in the readout pulse. The initial state of the spins before experiencing the first pulse was assumed to be unsaturated with only a vertical component. The presence of a 90° pulse placed the vertical (transverse) component existing immediately before the pulse into the transverse (− vertical) component, while the presence of a 180° pulse placed the vertical (transverse) component into the − vertical (− transverse) component. The vertical and horizontal states of each elemental volume were updated throughout the array using standard exponential decay models with decay rates of T_1 and T_2, respectively.[12] For each velocity the final echo amplitude at readout was computed by the signed summation of the transverse components of each of the discrete volume elements.

III. FLOW PHANTOM AND METHODS

In order to experimentally validate the results of the flow model, the phantom of Fig. 2 was constructed from nonmagnetic materials, primarily Lucite. It consists of a rotating cylinder 25 cm in diameter and 4 cm in width mounted on a base containing gears and a turbine driven by a jet of compressed air. The rotating cylinder was filled with manganese chloride solution (T_1 = 840 ms, T_2 = 100 ms) with relaxation times chosen to mimic human blood at 0.35 T. The cylinder is nearly bisected by a thin septum less than 1 mm thick to guarantee static flow within the cylinder during rotation. At the center of the cylinder is a Lucite rod which runs be-

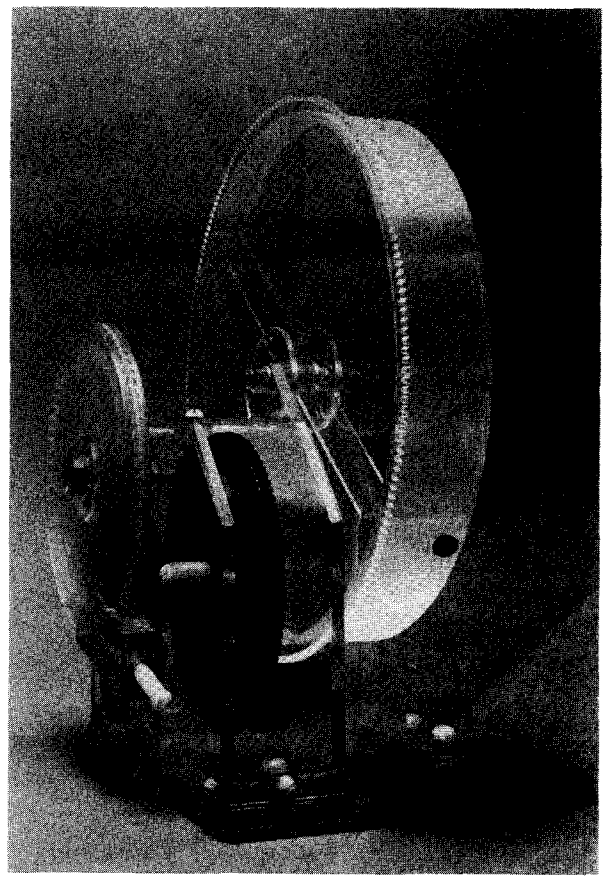

FIG. 2. Bulk flow phantom consisting of a rotating cylinder 25 cm in diameter and 4 cm in width filled with manganese chloride solution and mounted on a base containing gears and a turbine driven by a jet of compressed air. The cylinder is bisected by a thin septum less than 1 mm thick to guarantee fluid stasis during rotation.

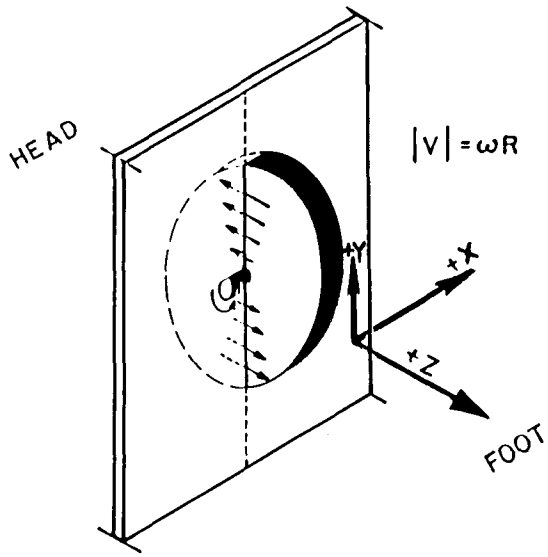

FIG. 3. Schematic of bulk flow phantom in magnet showing the transaxial orientation of the imaged plane. In the Diasonics scanner the z axis is directed along the bore of the magnet towards the foot of the patient, the x axis is directed laterally towards the left of the supine patient, and the y axis is directed vertically, i.e. ventrally, with respect to the supine patient.

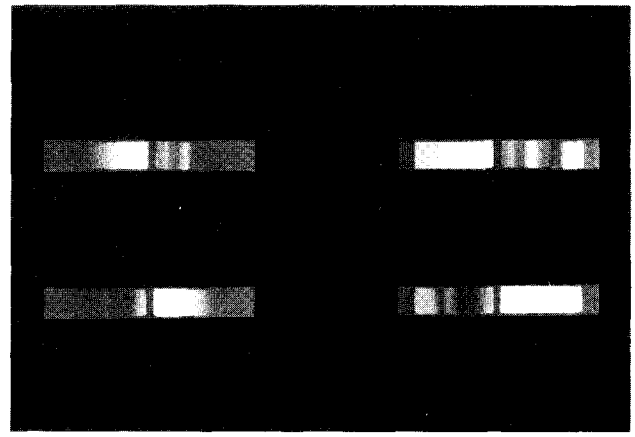

FIG. 4. Acquired transaxial images through the center of the rotating phantom using a spin-echo sequence of $T_r = 0.5$ s and $T_e = 28$ and 56 ms. The first echo is on the left and the second echo is on the right for both slice 1 (top) and 5 (bottom). In all cases the top of the phantom is on the left and shows effects of negative z-axis velocities and the bottom shows effects of positive velocities. The cylinder hub produces no MR signal and is dark.

tween the parallel surfaces and helps to locate the center of rotation of the cylinder during imaging. With the rotating phantom placed on the patient bed in the magnet such that the axis of rotation is the intersection of the transverse and coronal planes, a single transverse image acquisition through the axis of rotation yields a plot of magnetic resonance (MR) image intensities for a linear spectrum of velocities along the z axis. As shown in Fig. 3 the magnitude of the velocity in the imaged transverse plane is proportional to the product of the distance from the axis of rotation and angular velocity in rad/s. The size of the imaging rf coil limits the size of the cylinder's radius, and the angular velocity is limited such that all unexcited z-axis spins are nearly at their steady state, unsaturated value, i.e., the period of one rotation is limited to always be longer than three T_1's of the imaged material. Under constraints imposed by our radius and the material's T_1, velocity effects up to $\pm$ 30 cm/s can be accurately observed. The angular velocity of the phantom is varied by changing the pressure head at the nozzle of the jet. Angular velocity is measured by timing the period required for ten revolutions both before and after imaging the phantom. Variations less than 3% were accepted and averaged to obtain the angular velocity.

Images were obtained using a Diasonics 0.35 T superconducting magnet using a vendor supplied, partial saturation, spin-echo sequence with a T_r of 0.5, and T_e's of 28 and 56 ms and with selective 180° refocusing pulses. Nominal slice thickness was 7 mm with 3-mm interslice gaps. Nominal pixel resolution was 1.7 mm. Transverse images of both the rotating and static phantom were made with the phantom's axis of rotation centered in the slice of interest by moving the patient bed. After both the static and rotating cases were imaged, the phantom was moved to the center of the adjacent slice and the process repeated until all slices of the multislice sequence were imaged. The top pair of images in Fig. 4 shows the first (left) and second echo (right) images of the rotating phantom for slice 1 of the five slice sequence. The bottom pair shows the same for slice 5. Following acquisition horizontal pixels from the interior of the phantom which were free of truncation-related reconstruction artifacts were averaged to obtain an experimental echo amplitude profile as a function of radius. Each rotating amplitude profile was normalized for variations in rf coil field strength by dividing the rotating profile by the corresponding median filtered, static profile. Iteratively applied 5 and 23 point median filters were used to reduce noise and eliminate the gap of the hub in the static reference image to prevent noise being divided by noise in the region of the hub. Figure 5 shows the static profile of slice 1 before (a, top) and after (b, bottom) median filtering. After normalization the amplitude profiles for each echo and slice combination were plotted as functions of velocity. Figure 6(a) shows the normalized experimental results from the flow phantom on the top row and the computer model results on the bottom row for slice 1 of a five slice sequence. Echo amplitude is plotted on the ordinate versus velocity on the abcissa. Results for first echo are in the left column while results for second echo are in right column. The gap at the center of the normalized experimental rotating profile is an artifact of the wheel hub and obscures results only for velocities very near zero. Figure 6(b) shows the results for slice 3, and Fig. 6(c) shows the results for slice 5. Results for the other two slices of the five slice sequence are just as easily plotted and are available upon request, but are omitted here for convenience. The model parameters used in the generation of Fig. 6 which visually gave the best overall fit across all of the slices were slice separation of 1 cm, 90° pulse width of 0.7 cm, and 180° pulse width of 1.0 cm.

The model ignores odd-echo dephasing effects which occur within a pixel due to shear, i.e., different velocities contributing to echo amplitude within a single pixel, typically experienced in laminar flow. The bulk flow phantom is also insensitive to odd-echo dephasing by design. Because the readout, or x axis, gradient is often on during the complete

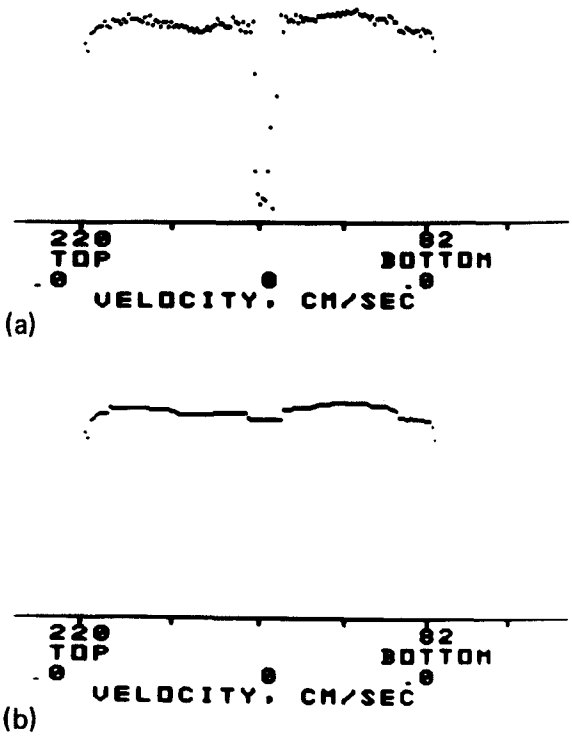

FIG. 5. Top profile (a) is taken from the first echo image of the static phantom with hub centered on slice 1. The application of a 23-point and 5-point median filter yields the bottom profile (b). Note that larger window median filter has removed the signal void associated with the hub. The bottom profile is used for normalizing profile taken from top, left image of Fig. 4.

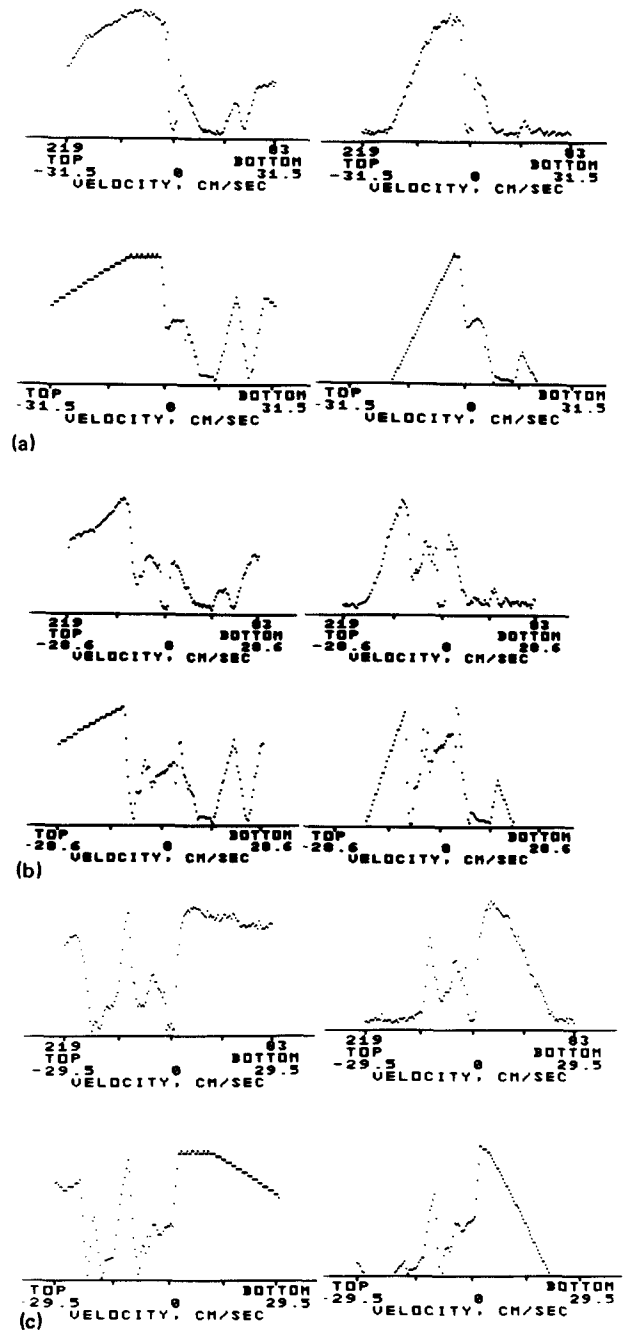

FIG. 6(a) Normalized experimental (top) and computer model (bottom) echo amplitudes for first (left) and second (right) echoes vs velocity in cm/s for slice 1 of five slice sequence. (b) Same as Fig. 6(a) for slice 3 of five slice sequence. (c) Same a Fig. 6(a) for slice 5 of five slice sequence.

period from 90° pulse to echo development, x-axis velocity components are typically the major contributors in clinical imaging situations to dephasing from shear. But with the phantom rotating entirely within the sagittal plane there are no x- or y-axis velocity components in the imaging plane. Any odd-echo dephasing is due to a z-axis velocity gradient along the radius of the phantom in the imaged transverse plane. Since the phase distribution of material contributing to one pixel is a function of the velocity distribution, the width of the velocity distribution for a pixel in the phantom is equal to product of the rate of variation of velocity with respect to radius and the width of a pixel. Since the z-axis velocity in the imaged transverse plane at any radius is the product of angular velocity and radius, the rate of variation of velocity with respect to radius, i.e. shear, is independent of radius and equal to the angular velocity. Thus the velocities contributing to one pixel have a uniform distribution about a mean, where the distribution width, ΔV, is equal to the product of angular velocity and pixel spacing. Since the duration of the z-axis gradient, which is used for transaxial slice selection during rf pulsing, is typically much shorter than the readout gradient, we can conservatively estimate the worst case dephasing by using the expression developed for readout gradient dephasing in the x-axis direction where the readout gradient is constantly applied during the interval from the first 90° pulse until readout, i.e.,

$$\Delta\phi = \gamma G(\Delta V)T_e^2/4\,, \qquad (1)$$

where $\Delta\phi$ is the width of the phase distribution, γ is the gyromagnetic ratio, G is the magnitude of the readout gradient, ΔV is the width of the velocity distribution, and T_e is the time to first echo.[13] For our z-axis gradient of 2 kHz/cm, T_e of 28 ms, pixel spacing of 1.7 mm, and a maximum angular velocity of 10 rev/25 s, the width of the uniform phase distribution is 0.17 rad. Such a worst case dephasing distribution will reduce the expected amplitude equally at all phantom radii by only 0.12%.

Note that while the model addresses one-dimensional, constant velocity motion, the bulk flow phantom only approximates the condition of constant velocities. No attempt is made here to increase the complexity of the model's equation of motion to incorporate such disparity, although such

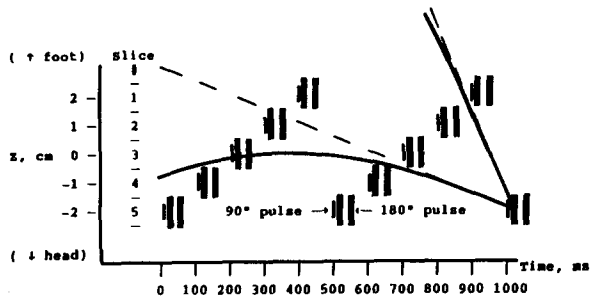

FIG. 7. Pulse position-timing diagram for five slice sequence showing actual (solid lines) trajectories of material with phantom rotating at an angular velocity of 1 rev/2.4 s. Ideal, i.e., lines of constant velocity are illustrated by the dashed lines.

an approach is possible. Instead we simply develop an error criterion for the phantom such that if the criterion is made sufficiently small, then the phantom results approach those of the constant velocity model. Since the flow phantom is based on a rotating wheel, the z-axis motion of the material that passes through the rephasing pulse of the slice of interest is sinusoidal. With the hub of the phantom centered in the slice of interest the loci of material for a family of different velocities describes a family of sinusoidal positions with respect to time, $z(t)$, each of which pass through the refocusing pulse with different slope or velocity, $v_z(0)$, where $t=0$ is arbitrarily chosen to be the time of occurrence of the desired refocusing pulse for the purposes of this discussion, i.e.,

$$z(t) = \pm r \sin \omega t , \tag{2}$$

where the radius, r, of the wheel is bounded by $0 \leqslant r \leqslant R_{\max}$ and ω is the angular velocity, and

$$v_z(t) = z'(t) = \pm \omega r \cos \omega t . \tag{3}$$

If we let the normalized velocity error of the material during one repetition of the imaging sequence be constrained to some upper threshold we get

$$|e(t)|/\omega r = |[\omega r - z'(t)]|/\omega r$$
$$= |1 - \cos \omega t| \leqslant |e_{\max}|, \quad \text{for } -T_r \leqslant t \leqslant 0 , \tag{4}$$

where $T_r = NT_i$, T_i is the interval between 90° pulses in the multislice sequence, and N is the number of slices in the sequence. Then by using a Taylor expansion of the cosine term and ignoring the contributions of all terms above the second derivative we can write the following approximation:

$$|1 - \cos \omega t| = (\omega t)^2/2 \leqslant e_{\max} . \tag{5}$$

By substituting the design goal of

$$\omega = V_{\max}/R_{\max} , \tag{6}$$

where $V_{\max}$ is the maximum velocity of interest, we obtain

$$(NT_i V_{\max}/R_{\max})^2 \leqslant |e_{\max}| . \tag{7}$$

Hence $(NT_i V_{\max}/R_{\max})$ is a good candidate for a quantitative figure of error, the opposite of a figure of merit, and should be minimized in the design process. Obviously this requires $R_{\max}$ to be as large as possible and still fit within the rf coil. As we mentioned earlier this design goal is also subject to the constraint that the unpulsed rotating material must have sufficient time to remain relaxed, i.e., the period of one rotation should exceed $3T_1$ of the material. Shown in Fig. 7 are two curves plotted for our maximum angular velocity of 1 rev/2.4 s. By comparing the desired, dashed straight lines with the actual, solid curves, it is clear for the case of the five slice sequence that the results of the lower velocities are compromised more than the higher ones, and the experimental determination of lower velocity effects should be performed using lower angular velocities. The use of 10 or 20 slice imaging sequences would require a new phantom design using a larger radius wheel operated at a lower angular velocity. Note that when $(NT_i V_{\max}/R_{\max})$ is sufficiently small, the rotating phantom is capable of generating a good, constant z-axis velocity approximation because both $z''(t)$ and the vertical (y axis) velocity component are zero in the imaged plane of the hub.

IV. CONCLUSIONS

A generalized technique of computing quantitative estimates of echo strengths for bulk flows has been presented. Although the experimental results presented in this paper apply specifically to the Diasonics 3.5 T imager, the modeling technique is applicable to most imaging sequences by simply applying the appropriate imaging sequence parameters to fill the pulse-position graph.

In general note that echo amplitude peaks in the experimental results correspond to velocities, i.e. lines, in Fig. 1 for the selected slice in which the flowing material either experiences no previous 90° rf pulse and has therefore fully recovered, or if it is affected by prior 90° pulses, they occur with at longer intervals than the T_r experienced by the stationary material. For slices 4 or 5 at higher negative velocities some material even experiences an inversion-recovery sequence, i.e., 180° inversion pulse followed by a 90° readout pulse and a 180° refocusing pulse! Obviously 10 and 20 slice sequences have even more velocity dependent amplitude peaks than the five slice sequence demonstrated here.

As seen from the generally good agreement between the experimental results and those of the model, most of the assumptions of the model are justified. General improvement in the performance of the model, especially affecting the shape of the response for negative velocities in slice 1 and positive velocities in slice 5, could be obtained by allowing the refocusing pulse to have a more realistic flip angle profile instead of the rectangular profile used here. It is worth noting that the gross features of the experimental results are fit reasonably well using only 90° pulses in the model,[14] while the finer features at higher velocities are better fit by the incorporation of the 180° readout pulses in the model.

An instructive example of the formation of a typical flow amplitude profile seen in MR is demonstrated in Fig. 8 and is included as an important part of the conclusions of this paper. Assume that flow in the inferior vena cava has the classical parabolic profile shown in Fig. 8(a). Flow directed toward the head is in the negative z direction. Assume the flow profile is observed in one of the echoes of slice 3 from a five slice sequence resulting in the approximate relationship of echo amplitude versus velocity demonstrated by Fig. 8(b) for negative velocities. Now by mapping the velocity at each radius in Fig. 8(a) to an amplitude via Fig. 8(b) we derive the amplitude flow profile seen as the solid line in Fig. 8(c). If the flow profile was observed in an even echo image then

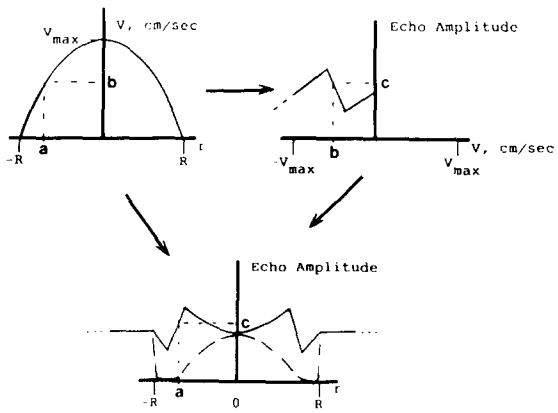

FIG. 8. Example of amplitude profile generation across a tubular vessel having classical parabolic flow.

because of even echo rephasing the result of Fig. 8(c) is complete and should accurately represent the profile. However if the image was from an odd echo, the effects of shear-induced dephasing must be taken into account. For laminar flow in a circular tube recall that shear, i.e.,

$$\left|\frac{\partial v}{\partial r}\right| = \frac{2V_{\max} r}{R^2}, \tag{8}$$

is greatest at the edge of the vessel, i.e. $r = R$, and has the most deleterious effect on echo amplitudes. Note that there is no shear at the center of the vessel and therefore no reduction in echo amplitude. The resultant flow profile for an odd echo might appear as the dotted line in Fig. 8(c). Calculation of the dephasing effect is relatively complicated and requires detailed knowledge of the z gradient waveform in order to compute the dephasing and resulting decrease in odd- echo amplitude.

The described ringed flow profiles are rarely seen in arteries due to temporal averaging of pulsatile and sometimes turbulent flow, but are more prevalent in venous flow.[14] In addition the partial volume summation of the effects of a range of velocities represented by one pixel in regions of high shear markedly reduces the number of velocity rings observed.

In summary any velocity vector can be decomposed into its three orthogonal components. Flow along the x axis, e.g., the frequency readout direction in the typical two-dimensional Fourier reconstruction technique, has its position faithfully preserved at time of readout, but can suffer amplitude loss from odd-echo dephasing due to shear effects in the x-axis direction. Flow along the y axis, e.g., the phase encoding direction, while subject to smaller losses in odd-echo amplitude from the dephasing effects of shear which occur during the smaller duration of the phase encoding gradient, is erroneously displaced along the y axis due to phase errors inherited from y-axis motion occurring between the phase encoding pulse and readout. Flow along the z axis has been thoroughly described in the preceding paragraphs. The model presented herein includes both the single slice effects previously well described by others, as well as multislice effects experienced in standard, vendor supplied sequences. The single slice effects predicted by the model (without first echo dephasing) are seen in negative velocities for slice 1, Fig. 6(a), and positive velocities for slice 5, Fig. 6(c). For these portions of the model results, previously unexcited spins are entering the readout slice, which is the same situation that occurs in a single slice sequence. Note that the model shows a rapid increase in echo amplitude to levels more than double the static value as the absolute value of velocity increases slowly from zero, previously referred to as "paradoxical enhancement." After a plateau in echo amplitude (due to the difference in widths of the 90° and 180° pulse), the amplitude begins a linear decrease with respect to velocity due to the partial volume relationship between the region stimulated by the 90° pulse and the 180° readout pulse.

It should be clear that because of the multivalued relationship between velocity and echo amplitude in any slice of a standard, multislice sequence, it is very difficult, if not absolutely impossible, to relate spatially averaged amplitudes taken over the lumen of a vessel to quantitative flow. Thus we look forward to the introduction and validation of quantitative angiographic sequences in clinical MRI.

We feel that both the model and the flow phantom possess value beyond that demonstrated for these circumstances. The modeling technique can easily encompass other pulse sequences and provide valuable insight, while the flow phantom can be used to assess quantitative accuracy of newly emerging flow selective sequences.

ACKNOWLEDGMENTS

The authors thank Quentin Westrick for his skillful construction of the flow phantom, J. A. Borrello and R. J. Schreiner for aid in data acquisition, and Alex M. Aisen and Thomas L. Chenevert for their helpful suggestions.

[1] L. Axel, Am. J. Roentgenol. **143**, 1157 (1984).
[2] W. G. Bradley, Jr., V. Waluch, K. Lai, E. J. Fernandez, and C. Spalter, Am. J. Roentgenol. **143**, 1167 (1984).
[3] P. R. Moran, Magn. Reson. Imaging **1**, 197, (1982).
[4] M. O'Donnell, Med. Phys. **12**, 59 (1985).
[5] K. Shimizu, T. Matsuda, T. Sakurai, A. Fujita, H. Ohara, S. Okamura, S. Hashimoto, H. Mano, C. Kawai, and M. Kiri, Radiology **159**, 195 (1986).
[6] L. Axel, A. Shimakawa, and J. MacFall, Magn. Reson. Imaging **4**, 199 (1986).
[7] C. L. Dumoulin and H. R. Hart, Radiology **161**, 717 (1986).
[8] F. W. Wehrli, A. Shimakawa, G. T. Gullberg, and J. R. MacFall, Radiology **160**, 781 (1986).
[9] P. E. Valk, J. D. Hale, L. E. Crooks, L. Kaufman, M. S. Roos, D. A. Ortendahl, and C. B. Higgins, Am. J. Roentgenol. **146**, 931 (1986).
[10] H. Hricak, E. Amparo, M. R. Fisher, L. Crooks, and C. B. Higgins, Radiology **156**, 415 (1986).
[11] P. M. Joseph, L. Axel, and M. O'Donnell, Med. Phys. **11**, 772 (1984).
[12] R. L. Dixon and K. E. Ekstrand, in *NMR in Medicine: The Instrumentation and Clinical Applications*, edited by S. R. Thomas and R. L. Dixon (American Institute of Physics, New York, 1986), pp. 1–31.
[13] L. Axel, Am. J. Roentgonal. **143**, 1161 (1984).
[14] D. M. Williams, C. R. Meyer, and R. J. Schreiner, "Flow effects in multislice spin-echo magnetic resonance imaging model, experimental verification and clinical examples," Invest. Radiol. **22**, 642 (1987).